

Aging power spectrum of membrane protein transport and other subordinated random walks

Zachary Fox

Los Alamos National Laboratory

Eli Barkai

Bar-Ilan University

Diego Krapf (✉ diego.krapf@colostate.edu)

Colorado State University <https://orcid.org/0000-0002-2833-5553>

Article

Keywords: single-particle tracking, spectral density, Wiener-Khinchin theorem

Posted Date: March 19th, 2021

DOI: <https://doi.org/10.21203/rs.3.rs-286804/v1>

License: © ⓘ This work is licensed under a Creative Commons Attribution 4.0 International License.

[Read Full License](#)

Version of Record: A version of this preprint was published at Nature Communications on October 25th, 2021. See the published version at <https://doi.org/10.1038/s41467-021-26465-8>.

Aging power spectrum of membrane protein transport and other subordinated random walks

Zachary R. Fox,^{1,2} Eli Barkai,³ and Diego Krapf^{1,4}

¹*School of Biomedical Engineering, Colorado State University, Fort Collins, Colorado 80523, U.S.A.*

²*The Center for Nonlinear Studies and Computational and Statistical Sciences Division,
Los Alamos National Laboratory, Los Alamos, New Mexico 87545, U.S.A.*

³*Department of Physics, Institute of Nanotechnology and Advanced Materials, Bar Ilan University, Ramat-Gan 52900, Israel*

⁴*Electrical and Computer Engineering, Colorado State University, Fort Collins, Colorado 80523, U.S.A.**

(Dated: February 28, 2021)

Single-particle tracking offers detailed information about the motion of molecules in complex environments such as those encountered in live cells, but the interpretation of experimental data is challenging. One of the most powerful tools in the characterization of random processes is the power spectral density. However, because anomalous diffusion processes in complex systems are usually not stationary, the traditional Wiener-Khinchin theorem for the analysis of power spectral densities is invalid. Here, we employ a recently developed tool named aging Wiener-Khinchin theorem to derive the power spectral density of fractional Brownian motion coexisting with a scale-free continuous time random walk, the two most typical anomalous diffusion processes. Using this analysis, we characterize the motion of voltage-gated sodium channels on the surface of hippocampal neurons. Our results show aging where the power spectral density can either increase or decrease with observation time depending on the specific parameters of both underlying processes.

I. INTRODUCTION

The power spectral density (PSD) of a signal contains important information and it is one of the most widely used characterization tools of deterministic and random processes. Traditionally, the PSD of a time-dependent signal $x(t)$ is defined in the limit of infinite time as

$$\langle S(\omega, \infty) \rangle = \lim_{t_m \rightarrow \infty} \frac{1}{t_m} \left\langle \left| \int_0^{t_m} e^{i\omega t} x(t) dt \right|^2 \right\rangle, \quad (1)$$

where the angle brackets denote averaging over an infinitely large ensemble, i.e., the expected value. In practice, when analyzing either experiments or numerical simulations, one does not have access to infinite measurement time, nor to a large ensemble of trajectories, and the PSD is estimated by using the periodogram. Thus, for a signal observed over a finite measurement time t_m , we deal with a PSD that can be a function of both frequency and measurement time, $S(\omega, t_m)$. For stationary processes, the PSD can be directly calculated from the autocorrelation function, $C(\tau) = \langle x(t)x(t+\tau) \rangle$, using the relation provided by the Wiener-Khinchin theorem [1]. Namely, this theorem states that the PSD is the Fourier transform of the autocorrelation function. However, there is growing interest in a wide class of non-stationary processes with scale invariant correlation functions. In these systems, the autocorrelation function explicitly depends on time, $C(\tau, t) = \langle x(t)x(t+\tau) \rangle = t^\gamma \phi_{\text{EA}}(\tau/t)$, and hence they are considered to exhibit aging. The Wiener-Khinchin theorem is invalid for non-stationary processes, which led to the development of a new theoretical framework, termed the aging Wiener-Khinchin theorem [2–4]. The PSD that emerges in these cases is, in turn, directly related to one over f noise.

Spectra of the one over f type are often found for low frequencies and many of its aspects are universal [5–8]. More generally, it is found that the PSD behaves like $1/\omega^\beta$, where the exponent $0 < \beta < 2$ contains information about the statistical properties of the process [9–13]. These spectra have been observed in systems as diverse as quantum dots [14, 15] and other low dimensional devices [16], nanopores [17], superconducting devices [18], nanoelectrodes [19], network traffic [20], earthquakes [21], DNA base sequences [22], and ecology [23]. In some of these examples, e.g. quantum dots [15], growing interfaces of the Kardar-Parisi-Zhang universality class [13], and vertical-cavity surface-emitting lasers [24], aging effects are also observed and the PSD depends on the measurement time, even when the measurement time is long. Thus, it is critical to understand how to analyze the PSD in aging processes. The PSD is currently emerging as a key tool in the characterization of random trajectories in biological systems because it

* diego.krapf@colostate.edu

35 informs on features that are difficult to infer using other traditional statistics. The main interest is in the study of the
 36 diffusive motion of individual molecules, taking advantage of developments in single-particle tracking [25–29]. With
 37 the goal of understanding the properties of individual trajectories, the PSD of stochastic processes gained renewed
 38 interest, for example with respect to the fluctuations of PSD estimator from a single trajectory [12, 30–34].

39 In the context of living cells, an open question remains whether we can observe aging effects in the PSD of relevant
 40 experiments. The dynamics of proteins (described by their position as a function of time) are broadly observed
 41 to exhibit antipersistent motion while also interacting with heterogeneous partners leading to immobilization times.
 42 Often, the immobilization times display heavy-tailed distributions leading to aging and ergodicity breaking. A useful
 43 way to model such diffusive transport is via the combination of two well-known stochastic processes [35, 36]: the
 44 continuous time random walk (CTRW) and fractional Brownian motion (fBM). Technically the marriage of these
 45 widely observed models is made possible with a subordination technique [37–39]. Briefly, in a subordination scheme,
 46 the steps of a random walk take place at operational times t_i defined by a directing stochastic process. For example,
 47 antipersistent motions such as diffusion in a fractal environment or fractional Brownian motion (fBM) with heavy-
 48 tailed immobilization times have been observed in mammalian cells in the motion of ion channels [40], insulin granules
 49 [41], membrane receptors [42], and nanosized objects in the cytoplasm [43], as well as for tracer particles in actin
 50 networks *in vitro* [44]. Subordinated processes are widespread beyond the dynamics in the cell [10, 13, 24, 45]. Systems
 51 with a heavy-tailed distribution of immobilization times exhibit aging in the sense that the observed statistical
 52 properties depend on how much time has passed since the preparation of the system. In practice, when the expected
 53 value of the immobilization times diverges, the only available characteristic time is the measurement time. As a
 54 consequence, quantities such as the autocorrelation function and the power spectral density depend on measurement
 55 time.

56 Here, we address the spectral content of subordinated processes with scale free immobilization times. The essence
 57 of our work is that one over f noise is represented by the power law relation $S(w) \sim A/\omega^\beta$, but, unlike standard
 58 approaches, the amplitude A depends on the measurement time. Our work has two aspects: On one hand, we want
 59 to find how the exponent β depends on the properties of the scale free process. On the other hand, we study how
 60 the amplitude A depends on measurement time t_m . If $A(t_m)$ is a decreasing function, the fluctuations effectively
 61 decrease with time, while if $A(t_m)$ is an increasing function, the noise level effectively increases with time. In the
 62 first part of our work, we analyze theoretically the power spectrum of subordinated processes using the aging Wiener-
 63 Khinchin theorem. We then focus on the analysis of the motion of voltage-gated sodium channels (Nav) on the somatic
 64 membrane of hippocampal neurons. Nav channels in the soma play important roles in the transfer of information
 65 to the rest of the neuron [46] and, therefore, their localization and dynamics have high physiological relevance. Our
 66 work not only validates the aging Wiener-Khinchin theorem as an emerging tool in spectral analysis, but it also sheds
 67 light on the exponents describing the aging and the frequency domain. The assumption that $1/f^\beta$ noise is described
 68 by a single exponent (β) is shown experimentally to be invalid. Furthermore, we show how the analysis of the PSD
 69 provides information on the exponents describing the time averaged mean square displacement, thus validating the
 70 model with independent measurements.

71 This article is organized as follows. After introducing the model, we use the aging Wiener-Khinchin theorem to
 72 obtain the PSD of subordinated random walks and gain a deeper understanding of the motion of ion channels on the
 73 plasma membrane of mammalian cells. We study the CTRW [47, 48], i.e., the classical subordination to Brownian
 74 motion, and fBM with heavy-tailed immobilization times, i.e., the combination of fBM and CTRW. These processes
 75 constitute the quintessential diffusion processes with heavy-tailed immobilization times. We first derive analytically
 76 the ensemble-averaged ACF, we then obtain the time-average ACF and, from it, we calculate exact results for the PSD.
 77 Analytical results for ACF and PSD are validated using numerical simulations. The trajectories of Nav1.6 channels
 78 in the cell membrane show the appropriate behavior for the PSD. Importantly, relations between the exponents
 79 that characterize the mean squared displacement and the power spectrum are derived. The experimental data show
 80 agreement with these relations and, in turn, the power spectrum provides information on the statistics of the protein
 81 motion. The detailed characterization of the motion of sodium channels exemplifies the usefulness of our approach to
 82 quantify properties of random trajectories.

83 II. AGING WIENER-KHINCHIN THEOREM

84 In any stationary process, the PSD is related to the autocorrelation function (ACF) $C_{EA}(\tau) = \langle x(t)x(t+\tau) \rangle$ via
 85 the fundamental Wiener-Khinchin theorem. Throughout the manuscript we employ the subscripts EA and TA to
 86 denote ensemble averages and time averages, respectively. In stationary ergodic processes, the time and ensemble
 87 averaged correlation functions are identical in the long time limit (see definitions below), so $C_{EA}(\tau) = C_{TA}(\tau)$. The

88 Wiener-Khinchin theorem can then be used to obtain the PSD, namely

$$\langle S(\omega, \infty) \rangle = 2 \int_0^\infty C_{\text{EA}}(\tau) \cos(\omega\tau) d\tau. \quad (2)$$

89 However, diffusive processes are intrinsically non-stationary and thus the Wiener-Khinchin theorem is invalid. In
 90 recent years, power spectrum theory has been expanded with a tool called the aging Wiener-Khinchin theorem [2–4].
 91 This theorem covers a broad class of non-stationary processes that possess an autocorrelation function with the long-
 92 time asymptotic $C_{\text{EA}}(t, \tau) = \langle x(t)x(t+\tau) \rangle \sim t^\gamma \phi_{\text{EA}}(\tau/t)$. Such correlation functions are common [4, 49, 50] and they
 93 are called scale invariant. An alternative analysis of the autocorrelation function is performed in terms of its time
 94 average C_{TA} of individual trajectories, where

$$C_{\text{TA}}(t_m, \tau) = \frac{1}{t_m - \tau} \int_0^{t_m - \tau} x(t)x(t+\tau) dt. \quad (3)$$

95 with t_m being the measurement time. As mentioned above, for ergodic processes, C_{TA} converges to C_{EA} in the
 96 long time limit. However, when the process is not ergodic, such as a scale-free CTRW, C_{TA} of individual trajectories
 97 remain random variables even in the long time limit [51, 52]. Thus, one analyzes the ensemble-average of the TA-ACF,
 98 $\langle C_{\text{TA}}(t_m, \tau) \rangle$. Further, ergodicity breaking leads to a difference in the two averages, $\langle C_{\text{TA}}(t_m = t, \tau) \rangle \neq C_{\text{EA}}(t, \tau)$.
 99 Each of these formalisms (ensemble vs. time averages) has its own advantages and disadvantages. Nevertheless, when
 100 the number of trajectories is small and the measurement time is long, the time averages lead to better statistics and it
 101 is, thus, the more commonly used method in single-particle tracking. When $C_{\text{EA}}(t, \tau) = t^\gamma \phi_{\text{EA}}(\tau/t)$, the time-average
 102 ACF has also the scaling form $\langle C_{\text{TA}}(t_m, \tau) \rangle = t_m^\gamma \phi_{\text{TA}}(\tau/t_m)$ [2]. The scaling function $\phi_{\text{TA}}(\tau/t_m)$ is directly related
 103 to the ensemble average via the relation

$$\phi_{\text{TA}}(y) = \frac{y^{1+\gamma}}{1-y} \int_{\frac{y}{1-y}}^\infty \frac{\phi_{\text{EA}}(z)}{z^{2+\gamma}} dz, \quad (4)$$

104 where $y = \tau/t_m$, which implies $0 \leq y \leq 1$.

105 For a measurement time t_m the power spectrum can be only obtained for the discrete set of frequencies $\omega_k t_m = 2\pi k$
 106 with k being a non-negative integer. That is, the frequencies can be resolved down to $\Delta\omega = 2\pi/t_m$, which decays
 107 to zero in the limit of large measurement time t_m . The aging Wiener-Khinchin theorem relates the average power
 108 spectrum for this set of frequencies to the time-averaged autocorrelation function [2, 4],

$$\langle S(\omega, t_m) \rangle = 2t_m^{1+\gamma} \int_0^1 (1-y) \phi_{\text{TA}}(y) \cos(\omega t_m y) dy. \quad (5)$$

109 A relation between the PSD and the ensemble-averaged correlation function also exists, but we will employ the relation
 110 to the time average because of its more common use in single-particle tracking experiments.

111 III. SUBORDINATED RANDOM WALKS: GENERAL CONSIDERATIONS

112 We now present the subordination model that we evaluate. We consider a fBM-like process at discrete times,
 113 $n = 0, 1, 2, 3, \dots$, with Hurst exponent H , such that its autocorrelation function at the discrete times n is given by
 114 [53]

$$\langle x_n x_{n+\Delta n} \rangle = D [n^{2H} + (n + \Delta n)^{2H} - \Delta n^{2H}], \quad (6)$$

115 where the diffusion coefficient D is a scaling parameter with units of m^2 . Then we place this process under the
 116 operational time of a CTRW, so that the particle is immobilized during sojourn times with a heavy-tailed distribution.
 117 A CTRW describes, for example, energetic disorder where a particle has random waiting times at each trapping site
 118 [47, 54]. This energy landscape is such that the mean waiting-time diverges and it is, thus, scale free. A CTRW
 119 with scale-free waiting times has been initially applied successfully to model the electrical conduction in amorphous
 120 semiconductors [55] and, since then, it has reached a broad range of applications [29, 36, 56].

121 The operational times are defined by a random process $\{t_n\}$ with non-negative independent increments $\tau_n =$
 122 $t_n - t_{n-1}$. The time increments τ_n between renewals are, in the long time limit, asymptotically distributed according
 123 to a probability density function (PDF) [57]

$$\psi(\tau_n) \sim \frac{\alpha}{\Gamma(1-\alpha)} \frac{t_0^\alpha}{\tau_n^{1+\alpha}}, \quad (7)$$

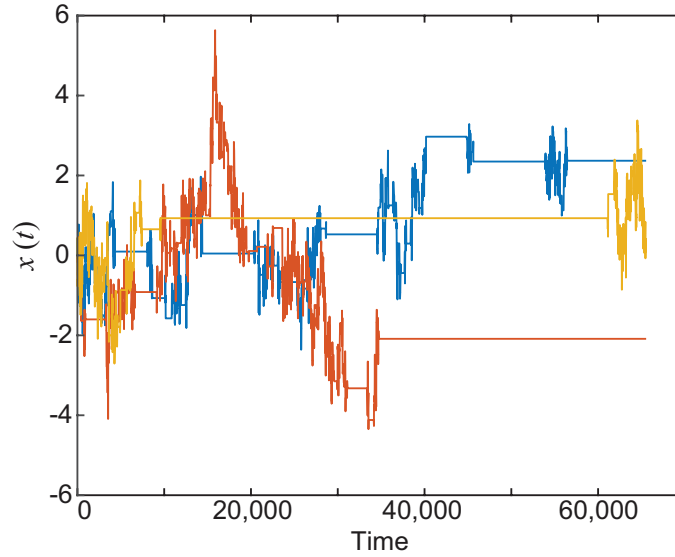


FIG. 1. Three representative trajectories for a process subordinated to fractional Brownian motion, such that the Hurst exponent is $H = 0.3$ and the CTRW anomalous exponent is $\alpha = 0.8$. Long immobilization times are observed within the fractional Brownian motion.

where $0 < \alpha < 1$, t_0 is a constant with units of time, and $\Gamma(\cdot)$ is the gamma function. At time t , the position of the particle is $x(t) = x_n$ where n is the random number of renewals in the interval $(0, t)$. Given n , x_n is determined by the discrete fBM process defined by Eq. 6. Three representative trajectories of such a process are shown in Fig. 1. The ensemble-averaged autocorrelation function of $x(t)$ is then

$$\begin{aligned} C_{\text{EA}}(t, \tau) &= \langle x(t)x(t+\tau) \rangle \\ &= \mathbb{E} [\mathbb{E} [x(t)x(t+\tau) | n_t; (n+\Delta n)_{t+\tau}]], \end{aligned} \quad (8)$$

124 where $\mathbb{E}[g(x)] = \langle g(x) \rangle$ represents the expected value of $g(x)$ and $\mathbb{E}[g(x)|y]$ is the conditional expected value of $g(x)$
 125 given y . In particular, the last term indicates the iterated expectation of $x(t)x(t+\tau)$, given that n steps have taken
 126 place up to time t and $n+\Delta n$ steps have taken place up to time $t+\tau$. The first expectation is taken on x_n and the
 127 second expectation on all possible values of n and Δn . Let us define $\chi_n(t)$ as the probability of taking exactly n steps
 128 up to time t . Further, we define $\chi_{n,\Delta n}(t, \tau)$ as the joint probability of taking n steps up to time t and Δn steps in
 129 the interval $(t, t+\tau)$.

Combining Eq. 8 and Eq. 6, we obtain

$$\begin{aligned} C_{\text{EA}}(t, \tau) &= \mathbb{E} [D (n_t^{2H} + (n+\Delta n)_{t+\tau}^{2H} - \Delta n_{\tau,t}^{2H})] \\ &= D \sum_{n=0}^{\infty} \sum_{\Delta n=0}^{\infty} (n^{2H} + (n+\Delta n)^{2H} - \Delta n^{2H}) \chi_{n,\Delta n}(t, \tau). \end{aligned} \quad (9)$$

130 Once the ensemble average autocorrelation function is found, we can obtain the time average $C_{\text{TA}}(t_m, \tau)$ via Eq. 4
 131 and, subsequently, the PSD using Eq. 5.

IV. CONTINUOUS TIME RANDOM WALK ($2H = 1$)

The fBM reverts to Brownian motion when $2H = 1$. In this case, the process is a traditional CTRW [47, 48]. The ensemble-averaged autocorrelation function in Eq. 9 is

$$\begin{aligned}
 C_{\text{EA}}(t, \tau) &= 2D \sum_{n=0}^{\infty} \sum_{\Delta n=0}^{\infty} n \chi_{n, \Delta n}(t, \tau) \\
 &= 2D \sum_{n=0}^{\infty} n \chi_n(t) = 2D \langle n(t) \rangle \\
 &\sim \frac{2D}{t_0^\alpha \Gamma(1 + \alpha)} t^\alpha,
 \end{aligned} \tag{10}$$

which, given the memoryless property of Brownian motion, boils down to the ensemble-averaged autocorrelation function being independent of lag time τ and equal to the mean squared displacement (MSD), $C_{\text{EA}}(t, \tau) = \langle x^2(t) \rangle$. In Eq. 10 we used the well know expression for the mean number of jumps in the interval $(0, t)$, $\langle n(t) \rangle$, valid at long times [57]. The MSD solution for the CTRW is $\langle x^2(t) \rangle \sim t^\alpha$, that is, it exhibits subdiffusion with anomalous exponent α .

The ensemble-averaged autocorrelation function in Eq. 10, for $2H = 1$, implies that $C_{\text{EA}} = t^\alpha \phi_{\text{EA}}$ with

$$\phi_{\text{EA}} = \frac{2D}{t_0^\alpha \Gamma(1 + \alpha)}, \tag{11}$$

i.e., ϕ_{EA} is a constant. Following Leibovich et al. [4], the time-averaged autocorrelation function is $\langle C_{\text{TA}} \rangle = t_m^\alpha \phi_{\text{TA}}(\tau/t_m)$ and, using Eq. 4, we can find the scaling function

$$\phi_{\text{TA}}(y) = \frac{2D}{t_0^\alpha \Gamma(2 + \alpha)} (1 - y)^\alpha, \tag{12}$$

where again we use $y = \tau/t_m$.

Next, we can use the time-averaged autocorrelation function in conjunction with the aging Wiener-Khinchin theorem to obtain the power spectral density of the CTRW. Given that the process time-averaged autocorrelation function has the form $\langle C_{\text{TA}}(t_m, \tau) \rangle = t_m^\alpha \phi_{\text{TA}}(\tau/t_m)$, we find the sample power spectral density by solving the integral in Eq. 5,

$$\begin{aligned}
 \langle S_{2H=1}(\omega, t_m) \rangle &= \frac{4Dt_m^{1+\alpha}}{t_0^\alpha \Gamma(2 + \alpha)} \int_0^1 (1 - y)^{1+\alpha} \cos(\omega t_m y) dy \\
 &= \frac{4Dt_m^{1+\alpha}}{t_0^\alpha \Gamma(3 + \alpha)} {}_1F_2 \left[1; \frac{3 + \alpha}{2}, \frac{4 + \alpha}{2}; - \left(\frac{\omega t_m}{2} \right)^2 \right],
 \end{aligned} \tag{13}$$

where ${}_1F_2(a; b_1, b_2; z)$ refers to the generalized hypergeometric function. The PSD in Eq. 13 is, as expected, a function of both frequency ω and realization time t_m . When $\alpha = 1$ the mean waiting time exists and the CTRW statistics revert in the long time to those of Brownian motion. In particular replacing $\alpha = 1$ and $\omega t_m = 2\pi k$ we find ${}_1F_2[1; 2, 5/2; -(\omega t_m)^2/4] = 6/(\omega t_m)^2$ and, thus, the PSD is that of standard Brownian motion, $\langle S(\omega) \rangle \sim \omega^{-2}$, independent of t_m . Expanding the hypergeometric function in Eq. 13 for $\omega t_m \gg 1$, it is found that the leading term scales in frequency as ω^{-2} and in time as $t_m^{-(1-\alpha)}$,

$$\langle S_{2H=1}(\omega, t_m) \rangle \sim \frac{4D}{t_0^\alpha \Gamma(1 + \alpha)} \frac{1}{t_m^{1-\alpha} \omega^2}, \tag{14}$$

which is related to the MSD via the relation

$$\langle S_{2H=1}(\omega, t_m) \rangle \sim \frac{2}{\alpha \omega^2} \frac{\partial}{\partial t_m} \langle x^2(t_m) \rangle. \tag{15}$$

While Eq. 15 applies to the CTRW, we will see later that it is not universal for the scale free processes under study. Figure 2 shows a comparison of these analytical results to numerical simulations of 10,000 realizations with $\alpha = 0.7$. The MSD exhibits a power law, $\langle x^2(t) \rangle \sim t^\alpha$ (Fig. 2a). The power spectral density is presented in Fig. 2b for five different measurement times from $t_m = 2^8$ to 2^{16} and compared to both the exact result involving the hypergeometric

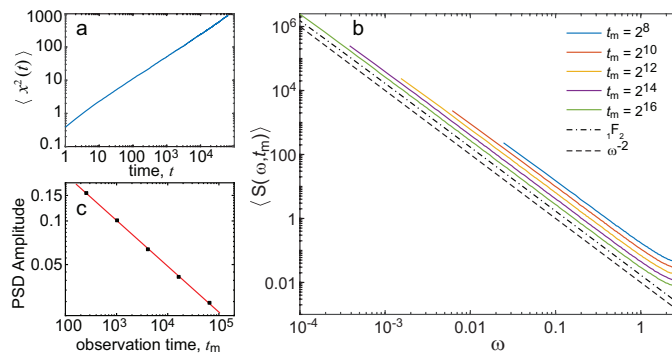


FIG. 2. Results from numerical simulation of the CTRW, i.e. Brownian motion with power-law waiting times. The simulations were performed for $\alpha = 0.7$ and 10,000 realizations were obtained. (a) MSD indicates subdiffusive behavior. A linear regression of $\log(\text{MSD})$ vs $\log(t)$ indicates $\langle x^2(t) \rangle \sim t^{0.69}$ (b) PSD at five different time exhibits aging. The hypergeometric exact solution is indicated with a dash dot line and the power law asymptotic $\sim \omega^{-2}$ is indicated with a dashed line. These two theoretical results are shifted down for clarity. (c) The amplitude $A(t_m)$ of the PSD, where $\langle S \rangle = A(t_m)/\omega^2$, shows $A(t_m) \sim t_m^{-0.31}$, which is the aging effect.

function ${}_1F_2$ and the power law asymptotic ω^{-2} . The two functions are very close when compared in a logarithmic scale and they agree with the numerical simulations. Specifically, at the smallest frequency, i.e., $\omega t_m = 2\pi$, the asymptotic form deviates from the exact result by a magnitude of 11% and when $\omega t_m = 2\pi \times 10$, this deviation reduces to 2%. The spectra also exhibit aging with an amplitude that scales as $t_m^{-(1-\alpha)}$ (Fig. 2c). Intuitively, as the measurement time is made longer, we encounter longer stagnation periods and, hence, the PSD decays with measurement time. Physically, this effect is due to the broadly distributed trapping times in the system.

V. PROCESS SUBORDINATED TO FBM ($0 < H < 1$)

A. Autocorrelation function

When $2H \neq 1$, the process has positively correlated increments for $H > 0.5$ and negatively correlated increments when $H < 0.5$. The autocorrelation function C_{EA} in Eq. 9 is

$$C_{\text{EA}}(t, \tau) = D [\langle n^{2H}(t) \rangle + \langle n^{2H}(t + \tau) \rangle - \langle \Delta n^{2H}(\tau; t) \rangle]. \quad (16)$$

where $\Delta n(\tau; t)$ is the number of steps between the aged time t and $t + \tau$. Using renewal theory and Eq. 7, the terms in Eq. 16 are found to be (see Supplementary Material)

$$\langle n^{2H}(t) \rangle = \frac{\Gamma(1 + 2H)}{t_0^\gamma \Gamma(1 + \gamma)} t^\gamma, \quad (17)$$

$$\langle \Delta n^{2H}(\tau; t) \rangle = \frac{\Gamma(1 + 2H)}{t_0^\gamma \Gamma(1 + \gamma)} b {}_2F_1 \left(1, 1 - \alpha; 2 - \alpha + \gamma; -\frac{\tau}{t} \right) t^{\alpha-1} \tau^{1-\alpha+\gamma}, \quad (18)$$

where ${}_2F_1(a_1, a_2; b; z)$ is the Gaussian hypergeometric function. We have defined

$$\gamma = 2\alpha H, \quad (19)$$

and the constant b is

$$b = \frac{\sin(\pi\alpha)}{\pi} \frac{\Gamma(1 - \alpha)\Gamma(1 + \gamma)}{\Gamma(2 - \alpha + \gamma)}. \quad (20)$$

Note that in the specific case that $2H = 1$, these constants revert to $b = \gamma = \alpha$. Using a different formalism, $\langle \Delta n^\nu(\tau; t) \rangle$ has been previously derived [58, 59]. These previous results were expressed in terms of incomplete beta functions but they are equivalent to ours. The ensemble-averaged autocorrelation function, Eq. 16, is thus given by

$$C_{\text{EA}}(t, \tau) = c_1 t^\gamma \left[1 + \left(1 + \frac{\tau}{t} \right)^\gamma - b {}_2F_1 \left(1, 1 - \alpha; 2 - \alpha + \gamma; -\frac{\tau}{t} \right) \left(\frac{\tau}{t} \right)^{1-\alpha+\gamma} \right], \quad (21)$$

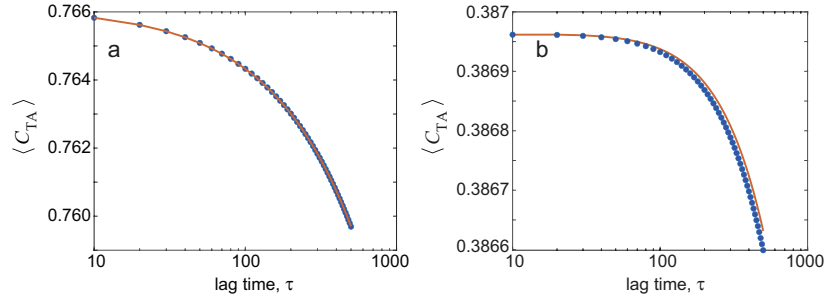


FIG. 3. Numerical simulations agree with the time average-autocorrelation analytical results. (a) Subdiffusive fBM example, with Hurst exponent $H = 0.3$ and sojourn times with power law distribution with $\alpha = 0.4$. (b) Superdiffusive fBM example, with Hurst exponent $H = 0.7$ and sojourn times with power law distribution with $\alpha = 0.4$. In both datasets, the realization time is $t_m = 2^{16}$ and the number of realizations is 10,000. The ACF is shown up to a lag time $\tau = 500$. The solid lines show analytical results given by Eq. 23, where $\langle C_{TA}(t_m, \tau) \rangle = t_m^\gamma \phi_{TA}(\tau/t_m)$.

165 with

$$c_1 = D \frac{\Gamma(1+2H)}{t_0^\gamma \Gamma(1+\gamma)}, \quad (22)$$

166 which gives the MSD when $\tau = 0$; $\langle x^2(t) \rangle = 2D \langle n^{2H}(t) \rangle = 2c_1 t^\gamma$.

167 The ensemble-averaged autocorrelation function in Eq. 21 has the form $C_{EA}(t, \tau) = t^\gamma \phi_{EA}(\tau/t)$, which implies
 168 the time-averaged autocorrelation function is of the form $\langle C_{TA}(t_m, \tau) \rangle = t_m^\gamma \phi_{TA}(\tau/t_m)$ [4]. Defining $y = \tau/t_m$ and
 169 following Eq. 4, we can find the scaling function

$$\phi_{TA}(y) = \frac{c_1}{1+\gamma} \left[(1-y)^\gamma + \frac{1}{1-y} - \frac{(1+\gamma)b}{\alpha} \frac{y^{1+\gamma-\alpha}}{(1-y)^{1-\alpha}} {}_2F_1 \left(1, -\alpha; 2-\alpha+\gamma; -\frac{y}{1-y} \right) \right]. \quad (23)$$

170 The analytical results for the time-averaged ACF (Eq. 23) were compared to numerical simulations. For this purpose,
 171 we performed simulations in MATLAB using the function *wfbm* to generate fBM. Subsequently the times between
 172 steps were drawn from a Pareto distribution $\psi(t) = \alpha t^{-(1+\alpha)}$ for $t \geq 1$. A total number of 10,000 realizations were
 173 obtained with $t_m = 2^{16}$ and a sampling time of 1. The numerical simulations are observed to agree with analytical
 174 results for both $H < 1/2$ and $H > 1/2$ in Fig. 3a and Fig. 3b, respectively.

175

B. Power spectral density

We see that the process subordinated to a fBM shows that $\langle C_{TA} \rangle = t_m^\gamma \phi_{TA}(\tau/t_m)$ with the time-average scaling
 correlation function $\phi_{TA}(\tau/t_m)$ given by Eq. 23. The aging Wiener-Khinchin theorem, Eq. 5, then gives the average
 power spectrum (see Supplementary Material),

$$\langle S(\omega, t_m) \rangle = 2c_1 t_m^{1+\gamma} \left[\frac{1}{(1+\gamma)(2+\gamma)} {}_1F_2 \left(1; \frac{3+\gamma}{2}, \frac{4+\gamma}{2}; -\left(\frac{\omega t_m}{2}\right)^2 \right) + \frac{b(1-\alpha+\gamma)\Gamma(1+\alpha)\Gamma(2-\alpha+\gamma)}{\alpha\Gamma(3+\gamma)} {}_2F_3 \left(\frac{2-\alpha+\gamma}{2}, \frac{3-\alpha+\gamma}{2}; \frac{3}{2}, \frac{3+\gamma}{2}, \frac{4+\gamma}{2}; -\left(\frac{\omega t_m}{2}\right)^2 \right) \right]. \quad (24)$$

By expanding these terms in the limit $\omega t_m \gg 1$ and noting that the spectrum is evaluated at frequencies $\omega t_m = 2\pi k$,
 we obtain the leading terms

$$\langle S(\omega, t_m) \rangle \approx 2c_1 t_m^{1+\gamma} \left[(\omega t_m)^{-2} + \frac{b \cos\left(\frac{\pi(\alpha-\gamma)}{2}\right) \Gamma(2-\alpha+\gamma)}{\alpha} (\omega t_m)^{-2+\alpha-\gamma} \right]. \quad (25)$$

176 Thus, the leading term for $\langle S(\omega, t_m) \rangle$ depends on the values of α and γ . In the case that $\alpha - \gamma > 0$,

$$\langle S_{2H<1}(\omega, t_m) \rangle \approx 2c_2 t_m^{-(1-\alpha)} \omega^{-2+\alpha-\gamma}, \quad (26)$$

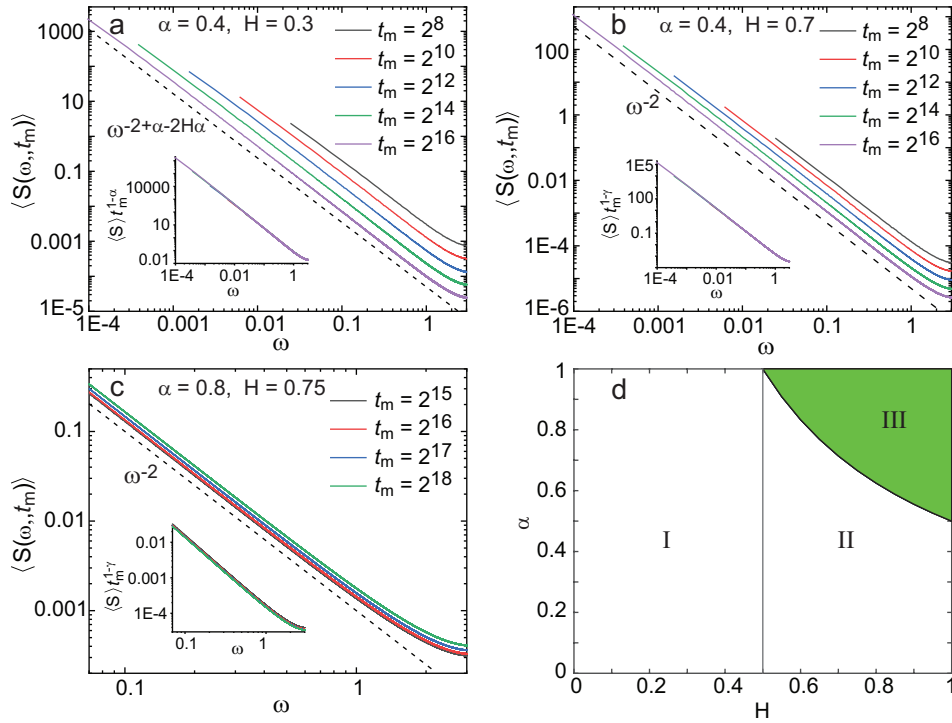


FIG. 4. Power spectral density of numerical simulations of fBM with heavy-tailed immobilization times. (a) Simulations for five different measurement times with $\alpha = 0.4$ and $H = 0.3$. The number of realizations is $N = 10,000$. Given that the fBM is subdiffusive ($H < 1/2$), the PSD is predicted to scale as $\langle S(\omega, t_m) \rangle \sim t_m^{-(1-\alpha)} \omega^{-2+\alpha-\gamma}$ as in Eq. 26. The dashed line shows the scaling $\omega^{-2+\alpha-\gamma}$. (Inset) When the PSD are multiplied by t_m^α , the five spectra are observed to collapse to a single master curve, validating the scaling prediction. (b) Simulations for five different measurement times with $\alpha = 0.4$ and $H = 0.7$, $N = 10,000$ realizations. The fBM is superdiffusive ($H > 1/2$) and the PSD is, thus, predicted to scale as $\langle S(\omega, t_m) \rangle \sim t_m^{-(1-\gamma)} \omega^{-2}$ (Eq. 28). The dashed line shows the scaling ω^{-2} . (Inset) When the PSD are multiplied by $t_m^{1-\gamma}$, the spectra collapse to a single curve. (c) Simulations for five different measurement times with $\alpha = 0.8$ and $H = 0.75$, $N = 5,000$ realizations. Given that $\gamma > 1$, the power spectrum increases with measurement time. The dashed black line indicates ω^{-2} . (Inset) Each power spectrum $\langle S(\omega, t_m) \rangle$ is multiplied by $t_m^{1-\gamma}$. The rescaled spectra converge to a universal curve at large t_m , but the convergence in this case is slow. (d) The shaded region (regime III) indicates the set of values for α and H that yields a PSD $\langle S(\omega, t_m) \rangle$ that increases with measurement time. In the rest of the plane, the power spectrum decays with t_m . Within this part of the plane, regime I is characterized by $\langle S(\omega, t_m) \rangle \sim t_m^{-(1-\alpha)} \omega^{-2+\alpha-\gamma}$ and regime II by $\langle S(\omega, t_m) \rangle \sim t_m^{-(1-\gamma)} \omega^{-2}$.

177 where

$$c_2 = \frac{c_1 b}{\alpha} \cos\left(\frac{\pi(\alpha - \gamma)}{2}\right) \Gamma(2 - \alpha + \gamma). \quad (27)$$

178 Note that $\gamma = 2\alpha H$ and thus $\alpha - \gamma > 0$ when $2H < 1$, i.e., this is the leading term when the fBM has a subdiffusive
179 nature. An example of this case is shown for numerical simulations with $\alpha = 0.4$ and $H = 0.3$ in Fig. 4a. The scaling
180 of the PSD both in t_m and ω agrees with Eq. 26.

181 When the underlying fBM is superdiffusive (i.e., $2H > 1$), $\alpha - \gamma < 0$ and the leading term is

$$\langle S_{2H>1}(\omega, t_m) \rangle \approx 2c_1 t_m^{-(1-\gamma)} \omega^{-2}. \quad (28)$$

182 This PSD is related to the mean square displacement in a similar way as the CTRW (Eq. 15), via the relation

$$\langle S_{2H>1}(\omega, t_m) \rangle \approx \frac{1}{\gamma \omega^2} \frac{\partial}{\partial t_m} \langle x^2(t_m) \rangle. \quad (29)$$

183 which is similar to Eq. 15, but with a factor $1/2$. When $2H > 1$, the power spectral density decreases with observation
184 time for small α and H , namely when $\gamma < 1$, i.e., $\alpha < 1/(2H)$. However, the PSD increases with measurement time
185 t_m when $\alpha > 1/(2H)$ as shown in Fig. 4d (shaded regime III). Figure 4b shows the power spectra for numerical
186 simulations where the underlying fBM is superdiffusive with $H = 0.7$ and $\alpha = 0.4$ which falls in the regime that

187 $\langle S(\omega, t_m) \rangle$ decays with t_m (regime II Fig. 4d). Figure 4c shows simulations with $H = 0.75$ and $\alpha = 0.8$ where
 188 $\langle S(\omega, t_m) \rangle$ increases with t_m . In this regime of increasing S , the convergence to Eq. 28 is very slow and appears to
 189 converge only for realization times $t_m > 10^5$. The increase of S with time is directly related to the fBM. It is observed
 190 that in the usual superdiffusive fBM without immobilizations, the PSD increases with time [32]. As immobilizations
 191 with a heavy tail distribution are considered, the increase with time seen for superdiffusive fBM is reduced and, if the
 192 heavy tail distribution decays to zero slowly enough, the trend is inverted back to the more traditional aging behavior
 193 where the PSD decays with measurement time.

194 The results in Fig. 4a-c are presented for the approximated asymptotic forms. Differences between the exact
 195 result (Eq. 24) and the asymptotic approximations (Eqs. 26 and 28) are substantial only at the lowest natural
 196 frequencies. At the natural frequency $\omega t_m = 2\pi$, the three specific analyzed cases, yield differences between the exact
 197 and approximated results of 23%, 20%, and 3% for Figs. 4a, b, and c, respectively and these differences reduce to
 198 7%, 6%, and 0.2% when $\omega t_m = 2\pi \times 10$, as shown in Supplementary Fig. 1. On a log-log plot, which is the common
 199 representation of $1/f$ type of spectra, these deviations are hard to detect.

200 What happens to the PSD in the limit $\alpha \rightarrow 1$? In this limit, the subordinated process behaves as the usual fBM and
 201 the PSD has a known form (see, e.g., [32]) such that $\langle S(\omega, t_m) \rangle \sim 1/\omega^{1+2H}$ when $2H < 1$ and $\langle S(\omega, t_m) \rangle \sim t_m^{2H-1}/\omega^{-2}$
 202 when $2H > 1$. The results shown in Eq. 26 and 28 approach these expressions when $\alpha \rightarrow 1$, given that $\gamma \rightarrow 2H$.
 203 A second interesting limit occurs when $2H \rightarrow 1$ (for any $0 < \alpha < 1$). In this limit, we recover the CTRW with
 204 $\langle S_{2H=1}(\omega, t_m) \rangle = 2(c_1 + c_2)/\omega^2$. This behavior is the same scaling presented in Eq. 14 because now $b = \alpha$ and $c_1 = c_2$.
 205 We note the factor $1/2$ between Eq. 15 and 29 arises because when $2H = 1$, the two leading terms converge to the
 206 same exponent.

207 VI. EXPERIMENTAL RESULTS

208 The derivation of the PSD of subordinated, correlated random walks enables us to characterize the motion of the
 209 voltage gated sodium channels Nav1.6 in the somatic plasma membrane of hippocampal neurons. Nav1.6 were tagged
 210 with an extracellular CF640R fluorophore via biotin-streptavidin and trajectories were obtained by single-molecule
 211 tracking. Experimental details have been published previously [60]. Live cells were imaged at 37 °C by total internal
 212 reflection fluorescence microscopy, and tracking of individual fluorophores was performed using the U-track algorithm
 213 [61]. We have previously found that somatic Nav1.6 channels transiently immobilized into cell surface nanodomains
 214 [60]. Further, we have found that the immobilization times were drawn from a heavy-tailed distribution, which
 215 caused the diffusion process to exhibit weak ergodicity breaking [62]. For this reason, we model the system using
 216 Eq. 7. An important property of heavy-tailed renewal processes is that they depend on the time that lapsed since
 217 the system started, and this time is denoted as the origin, $t = 0$ [63]. In the case of Nav channels, we start our
 218 measurements when the channel is delivered to the plasma membrane and, thus, the time $t = 0$ is well-defined.
 219 Besides immobilizations with a heavy-tailed distribution, Nav1.6 also show antipersistent fBM-like motion, leading to
 220 a non-linear time-averaged MSD. Here, we evaluate 87 Nav1.6 trajectories of 256 data points each, with a sampling
 221 time $\Delta t = 50$ ms.

222 Before digging into the PSD analysis of Nav channels, we consider their mean square displacement, which is a
 223 familiar statistical tool that helps us understand some basic properties of their motion. Figure 5a shows the ensemble-
 224 averaged MSD (EA-MSD, $\langle x^2(t) \rangle$) of the molecule positions and the ensemble-average of the time-averaged MSD
 225 (EA-TA-MSD) for three different observation times, $t_m = 64\Delta t$, $128\Delta t$, and $256\Delta t$. The EA-TA-MSD is defined in
 226 its usual way,

$$\langle \overline{\delta^2(\tau, t_m)} \rangle = \frac{1}{t_m - \tau} \left\langle \int_0^{t_m - \tau} [x(t + \tau) - x(t)]^2 dt \right\rangle, \quad (30)$$

227 where, using the same notation as in the autocorrelation function, τ denotes the lag time. The individual time traces
 228 of the time-averaged MSD $\overline{\delta^2(\tau, t_m)}$ scatter broadly [62] and, thus, we study the properties of their average rather
 229 individual trajectories. The large difference between the EA-TA-MSD and the EA-MSD (Fig. 5a) is a direct indication
 230 of ergodicity breaking in the motion of Nav channels [36, 62]. In the context of our model, the ergodic hypothesis
 231 breaks down since $\alpha < 1$ and, hence, the measurement time is smaller than the characteristic immobilization time.
 232 Ergodicity breaking is also the core reason behind the scattering of the individual time-averaged MSDs. The EA-TA-
 233 MSD of the subordinated process scales as [64]

$$\langle \overline{\delta^2(\tau, t_m)} \rangle \sim \frac{\tau^{1-\alpha+\gamma}}{t_m^{1-\alpha}}. \quad (31)$$

234 Figure 5a shows that the EA-TA-MSD indeed scales as $\langle \overline{\delta^2} \rangle \sim \tau^\lambda / t_m^{1-\alpha}$ with exponents estimated to be $\lambda = 1 - \alpha + \gamma =$
 235 0.82 ± 0.05 and $\alpha = 0.54 \pm 0.02$. If the PSD frequency exponent is smaller than 2 (regime I in Fig. 4d), Eq. 26 states

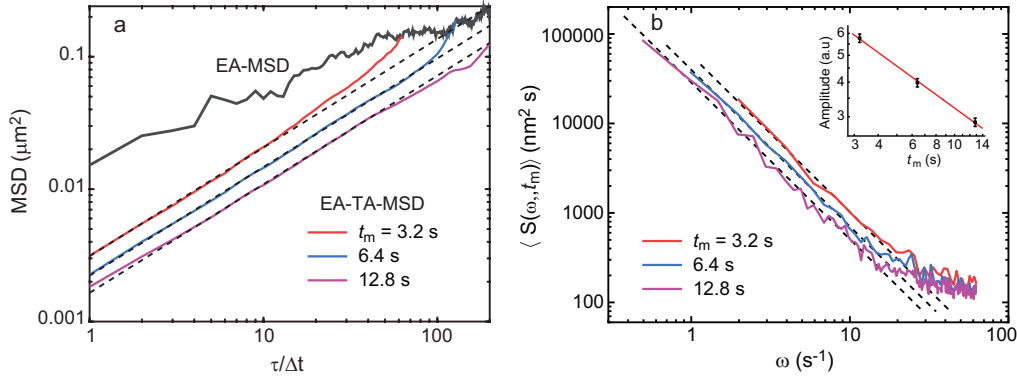


FIG. 5. Analysis of Nav1.6 experimental trajectories in the soma of hippocampal neurons. (a) The time-averaged MSD is different from the ensemble-averaged MSD (grey upper line). The time-averaged MSD scales as $\tau^{0.82 \pm 0.05}$ (dashed lines). The time averaged MSD decays with experimental time as $1/t_m^{1-\alpha}$, from which α is estimated to be 0.54 ± 0.02 . (b) Average spectra are presented for three measurement times. The dashed lines show a scaling $1/\omega^{1.75}$. Besides the power-law scaling, the spectra exhibit white noise evident at large frequencies, likely due to localization error. The inset shows the amplitude of the PSD as a function of measurement time in a log-log plot. It shows that the spectrum exhibits aging with a power law scaling $1/t_m^{1-\alpha}$, from which α is estimated to be 0.50 ± 0.02 .

236 that the PSD is directly related to the MSD exponents, $\langle S \rangle \sim 1/(t_m^{1-\alpha} \omega^{1+\lambda})$. Otherwise, when $H \geq 1/2$ (regimes II
237 and III), $\langle S \rangle \sim 1/(t_m^{1-\gamma} \omega^2)$.

238 The power spectrum of the Nav channel trajectories is shown in Fig. 5b. Performing measurements for the MSD
239 and the PSD we obtain their exponents independently. Since these statistical tools scale, respectively, as τ^λ and either
240 $1/\omega^{1+\lambda}$ or $1/\omega^2$, the comparison allows us to check the validity of the approach in the analysis of Nav channels. We
241 find that the PSD of Nav channels scales as a power law and it exhibits aging. The PSD decays with observation
242 time as predicted for a process with Hurst exponent $H < 1/2$ (see Eq. 26). Namely, $\langle S(\omega, t_m) \rangle \sim A(t_m)/\omega^{1.75 \pm 0.05}$.
243 This power law agrees with the predicted scaling of the PSD, $1/\omega^{1+\lambda}$, where λ is independently obtained using the
244 MSD. The PSD amplitude $A(t_m)$ as a function of measurement time t_m is shown in the inset of Fig. 5b, indicating
245 $A(t_m) \sim 1/t_m^{0.50 \pm 0.02}$, also in agreement with the dependence of the time-averaged MSD on experimental time.
246 According to Eq. 26, the PSD results imply $\alpha = 0.50 \pm 0.02$ and $H = 0.25 \pm 0.11$. The spectral analysis confirms the
247 predictions stating that the motion of Nav channels is a subordinated process and lets us obtain accurate estimates
248 of the waiting time distribution and the Hurst exponent from the PSD dependence on frequency and measurement
249 time. While the goal of this work pertained to the dynamics of proteins, it is directly applicable to any process where
250 a correlated random walk coexists with a non-ergodic CTRW.

251 VII. DISCUSSION AND CONCLUSIONS

252 The PSD of subordinated processes is found to be described in terms of hypergeometric functions (Eqs. 13 and 24).
253 However, it can be approximated to an excellent degree by simple power laws in the experimentally relevant frequency
254 range. This is especially true when the spectrum is plotted in a log-log scale, as is typically done in experiments on
255 $1/f$ noise (see Suppl. Fig. S1, for a quantitative evaluation). We characterize subordinated random walks via two
256 exponents, the Hurst exponent H and the exponent that describes the heavy-tailed waiting time distribution α . We
257 observe that it is possible to obtain α and H from the exponents that describe both the MSD and the PSD. Obtaining
258 equivalent results for these two vastly different metrics provides a strong validation of the subordinated process being
259 a valid model for the experimental system under consideration. The PSD depends on H in a piecewise manner.
260 When the parent process is a subdiffusive fBM, i.e., $H < 1/2$, the PSD scales in frequency as $\omega^{-2+\alpha-2\alpha H}$. On the
261 other hand, when the parent process is Brownian motion or superdiffusive fBM, i.e., $H \geq 1/2$ the scaling is ω^{-2} .
262 In the latter case, i.e., when $\langle S \rangle \sim \omega^{-2}$, the power spectrum is directly related to the time derivative of the MSD.
263 However, when $H < 1/2$, this relation is different. In this case, the scaling exponents of the time-averaged MSD and
264 the power spectrum are related via $\langle \delta^2 \rangle \sim \tau^\lambda$ and $\langle S \rangle \sim \omega^{-(1+\lambda)}$. The frequency scaling exponent is continuous in H
265 in the whole range and, thus, distinguishing between Brownian motion and subdiffusive fBM with H close to $1/2$ may
266 be difficult. Further, the frequency dependence when $H \geq 1/2$ is deceptively the same as that of normal Brownian
267 motion.

268 The PSD is found to exhibit aging, namely it depends on the experimental time t_m . This aging is observed in the

PSD scaling as $t_m^{-(1-\alpha)}$ for $H \leq 1/2$ and $t_m^{-(1-2\alpha H)}$ for $H > 1/2$. Again, we note that the aging exponent is piecewise linear and continuous in H . The difference in aging exponent regimes has been previously observed for a traditional fBM (without immobilizations), with a scaling $\langle S \rangle \sim t_m^{-(1-2H)}$ for $H > 1/2$ and no aging when $H \leq 1/2$ [32]. The subordinated scheme we studied here converges to the traditional fBM when $\alpha = 1$. In this particular case, $\alpha = 1$ implies the mean sojourn time during immobilizations exists and, as a consequence, the statistics of the subordinated process revert to those of the traditional fBM.

A particularly interesting feature of subordinated random walks is that the power spectrum can both increase or decrease with experimental time. When $H < 1/2$, the PSD always decays with t_m . However, when the fBM is superdiffusive, a competition is exerted between the two underlying stochastic processes: the PSD increases with t_m when the exponent α and the Hurst index H are such that $\alpha > 1/(2H)$ and, otherwise, the PSD decays (see Fig. 4d for a phase diagram).

In summary, we have derived the spectral content of a broad class of non-stationary diffusive processes using the aging Wiener-Khinchin theorem. This class of processes involves the coexistence of correlated fractional Brownian motion and power-law distributed sojourn immobilization times, which are encountered in vastly diverse scientific fields, such as hydrology [65, 66] and movement ecology [67]. The spectra exhibit $1/\omega^\beta$ behavior with an exponent β that depends on the characteristics of both underlying processes. In addition, it is found that the spectra exhibit aging in the measurement time. This analysis proved useful in elucidating the statistical properties of experimental trajectories in live mammalian cells obtained by single-particle tracking, opening a new avenue in the analysis of protein trajectories, which are known to exhibit highly complex behavior that often proves difficult to decipher.

ACKNOWLEDGEMENTS

The Nav1.6 imaging was performed by Dr. Elizabeth Akin. DK thanks Dr. Mike Tamkun for his help with the experiments and useful discussions. We acknowledge the support from the Colorado State University Libraries Open Access Research and Scholarship Fund (DK). The support of Israel Science Foundation's grant 1898/17 is acknowledged (EB).

-
- [1] R. Kubo, M. Toda, and N. Hashitsume, *Statistical physics II: nonequilibrium statistical mechanics*, Vol. 31 (Springer Science & Business Media, 2012).
- [2] N. Leibovich and E. Barkai, Aging Wiener-Khinchin theorem, *Phys. Rev. Lett.* **115**, 080602 (2015).
- [3] A. Dechant and E. Lutz, Wiener-Khinchin theorem for nonstationary scale-invariant processes, *Phys. Rev. Lett.* **115**, 080603 (2015).
- [4] N. Leibovich, A. Dechant, E. Lutz, and E. Barkai, Aging Wiener-Khinchin theorem and critical exponents of $1/f^\beta$ noise., *Phys. Rev. E* **94**, 052130 (2016).
- [5] P. Dutta and P. Horn, Low-frequency fluctuations in solids: $1/f$ noise, *Rev. Mod. Phys.* **53**, 497 (1981).
- [6] M. Weissman, $1/f$ noise and other slow, nonexponential kinetics in condensed matter, *Rev. Mod. Phys.* **60**, 537 (1988).
- [7] F. N. Hooge, $1/f$ noise sources, *IEEE Trans. Electron Devices* **41**, 1926 (1994).
- [8] I. Eliazar and J. Klafter, A unified and universal explanation for Lévy laws and $1/f$ noises, *Proc. Natl. Acad. Sci. U.S.A.* **106**, 12251 (2009).
- [9] B. Mandelbrot, *Gaussian self-affinity and fractals: globality, the Earth, $1/f$ noise, and R/S* , Vol. 8 (Springer Science & Business Media, 2002).
- [10] S. B. Lowen and M. C. Teich, Fractal renewal processes generate $1/f$ noise, *Phys. Rev. E* **47**, 992 (1993).
- [11] N. W. Watkins, Mandelbrot's $1/f$ fractional renewal models of 1963–67: The non-ergodic missing link between change points and long range dependence, in *International Work-Conference on Time Series Analysis* (Springer, 2016) pp. 197–208.
- [12] M. Niemann, H. Kantz, and E. Barkai, Fluctuations of $1/f$ noise and the low-frequency cutoff paradox, *Phys. Rev. Lett.* **110**, 140603 (2013).
- [13] K. A. Takeuchi, $1/f^\alpha$ power spectrum in the Kardar-Parisi-Zhang universality class, *J. Phys. A* **50**, 264006 (2017).
- [14] M. Pelton, D. G. Grier, and P. Guyot-Sionnest, Characterizing quantum-dot blinking using noise power spectra, *Appl. Phys. Lett.* **85**, 819 (2004).
- [15] S. Sadegh, E. Barkai, and D. Krapf, $1/f$ noise for intermittent quantum dots exhibits non-stationarity and critical exponents, *New J. Phys.* **16**, 113054 (2014).
- [16] A. A. Balandin, Low-frequency $1/f$ noise in graphene devices, *Nat. Nanotechnol.* **8**, 549 (2013).
- [17] R. M. Smeets, U. F. Keyser, N. H. Dekker, and C. Dekker, Noise in solid-state nanopores, *Proc. Natl. Acad. Sci. U.S.A.* **105**, 417 (2008).

- [18] J. Burnett, L. Faoro, I. Wisby, V. Gurtovoi, A. Chernykh, G. Mikhailov, V. Tulin, R. Shaikhaidarov, V. Antonov, P. Meeson, *et al.*, Evidence for interacting two-level systems from the $1/f$ noise of a superconducting resonator, *Nat. Commun.* **5**, 1 (2014).
- [19] D. Krapf, Nonergodicity in nanoscale electrodes, *Phys. Chem. Chem. Phys.* **15**, 459 (2013).
- [20] I. Csabai, $1/f$ noise in computer network traffic, *J. Phys. A* **27**, L417 (1994).
- [21] A. Sornette and D. Sornette, Self-organized criticality and earthquakes, *EPL (Europhys. Lett.)* **9**, 197 (1989).
- [22] R. F. Voss, Evolution of long-range fractal correlations and $1/f$ noise in DNA base sequences, *Phys. Rev. Lett.* **68**, 3805 (1992).
- [23] J. M. Halley and P. Inchausti, The increasing importance of $1/f$ -noises as models of ecological variability, *Fluct. Noise Lett.* **4**, R1 (2004).
- [24] M. A. Rodriguez, F. Denis-le Coarer, and A. Valle, $1/f$ noise in the intensity fluctuations of vertical-cavity surface-emitting lasers subject to parallel optical injection, *Phys. Rev. E* **97**, 042105 (2018).
- [25] S. Manley, J. M. Gillette, G. H. Patterson, H. Shroff, H. F. Hess, E. Betzig, and J. Lippincott-Schwartz, High-density mapping of single-molecule trajectories with photoactivated localization microscopy, *Nat. Methods* **5**, 155 (2008).
- [26] B. Biermann, S. Sokoll, J. Klueva, M. Missler, J. Wiegert, J.-B. Sibarita, and M. Heine, Imaging of molecular surface dynamics in brain slices using single-particle tracking, *Nat. Commun.* **5**, 1 (2014).
- [27] C. Manzo and M. F. Garcia-Parajo, A review of progress in single particle tracking: from methods to biophysical insights, *Rep. Prog. Phys.* **78**, 124601 (2015).
- [28] A. Huhle, D. Klaue, H. Brutzer, P. Daldrop, S. Joo, O. Otto, U. F. Keyser, and R. Seidel, Camera-based three-dimensional real-time particle tracking at kHz rates and Ångström accuracy, *Nat. Commun.* **6**, 1 (2015).
- [29] D. Krapf and R. Metzler, Strange interfacial molecular dynamics, *Physics Today* **72**, 48 (2019).
- [30] D. S. Dean, A. Iorio, E. Marinari, and G. Oshanin, Sample-to-sample fluctuations of power spectrum of a random motion in a periodic sinai model, *Phys. Rev. E* **94**, 032131 (2016).
- [31] D. Krapf, E. Marinari, R. Metzler, G. Oshanin, X. Xu, and A. Squarcini, Power spectral density of a single Brownian trajectory: what one can and cannot learn from it, *New J. Phys.* **20**, 023029 (2018).
- [32] D. Krapf, N. Lukat, E. Marinari, R. Metzler, G. Oshanin, C. Selhuber-Unkel, A. Squarcini, L. Stadler, M. Weiss, and X. Xu, Spectral content of a single non-Brownian trajectory, *Phys. Rev. X* **9**, 011019 (2019).
- [33] V. Sposini, R. Metzler, and G. Oshanin, Single-trajectory spectral analysis of scaled Brownian motion, *New J. Phys.* **21**, 073043 (2019).
- [34] V. Sposini, D. Grebenkov, R. Metzler, G. Oshanin, and F. Seno, Universal spectral features of different classes of random diffusivity processes, *New J. Phys.* (2020).
- [35] M. Magdziarz, A. Weron, K. Burnecki, and J. Klafter, Fractional Brownian motion versus the continuous-time random walk: A simple test for subdiffusive dynamics, *Phys. Rev. Lett.* **103**, 180602 (2009).
- [36] R. Metzler, J.-H. Jeon, A. G. Cherstvy, and E. Barkai, Anomalous diffusion models and their properties: non-stationarity, non-ergodicity, and ageing at the centenary of single particle tracking, *Phys. Chem. Chem. Phys.* **16**, 24128 (2014).
- [37] I. Sokolov, Lévy flights from a continuous-time process, *Phys. Rev. E* **63**, 011104 (2000).
- [38] B. Dybiec and E. Gudowska-Nowak, Subordinated diffusion and continuous time random walk asymptotics, *Chaos* **20**, 043129 (2010).
- [39] D. Krapf, Mechanisms underlying anomalous diffusion in the plasma membrane, in *Curr. Top. Membr.*, Vol. 75 (Elsevier, 2015) pp. 167–207.
- [40] A. V. Weigel, B. Simon, M. M. Tamkun, and D. Krapf, Ergodic and nonergodic processes coexist in the plasma membrane as observed by single-molecule tracking, *Proc. Natl. Acad. Sci. U.S.A.* **108**, 6438 (2011).
- [41] S. A. Tabei, S. Burov, H. Y. Kim, A. Kuznetsov, T. Huynh, J. Jureller, L. H. Philipson, A. R. Dinner, and N. F. Scherer, Intracellular transport of insulin granules is a subordinated random walk, *Proc. Natl. Acad. Sci. U.S.A.* **110**, 4911 (2013).
- [42] A. Mosqueira, P. A. Camino, and F. J. Barrantes, Cholesterol modulates acetylcholine receptor diffusion by tuning confinement sojourns and nanocluster stability, *Sci. Rep.* **8**, 1 (2018).
- [43] F. Etoc, E. Balloul, C. Vicario, D. Normanno, D. Liße, A. Sittner, J. Piehler, M. Dahan, and M. Coppey, Non-specific interactions govern cytosolic diffusion of nanosized objects in mammalian cells, *Nat. Mater.* **17**, 740 (2018).
- [44] M. Levin, G. Bel, and Y. Roichman, Different anomalous diffusion regimes measured in the dynamics of tracer particles in actin networks, arXiv preprint, arXiv:2011.00539 (2020).
- [45] R. Roman-Ancheyta, O. de los Santos-Sánchez, L. Horvath, and H. M. Castro-Beltrán, Time-dependent spectra of a three-level atom in the presence of electron shelving, *Phys. Rev. A* **98**, 013820 (2018).
- [46] M. H. Myoga, M. Beierlein, and W. G. Regehr, Somatic spikes regulate dendritic signaling in small neurons in the absence of backpropagating action potentials, *J. Neurosci.* **29**, 7803 (2009).
- [47] E. W. Montroll and G. H. Weiss, Random walks on lattices. II, *J. Math. Phys.* **6**, 167 (1965).
- [48] M. F. Shlesinger, Origins and applications of the Montroll-Weiss continuous time random walk, *Eur. Phys. J. B* **90**, 93 (2017).
- [49] J.-P. Bouchaud, Weak ergodicity breaking and aging in disordered systems, *J. Physique I* **2**, 1705 (1992).
- [50] J. Vollmer, L. Rondoni, M. Tayyab, C. Giberti, and C. Mejía-Monasterio, Displacement autocorrelation functions for strong anomalous diffusion: A scaling form, universal behavior, and corrections to scaling, *Phys. Rev. Res.* **3**, 013067 (2021).
- [51] G. Margolin and E. Barkai, Nonergodicity of blinking nanocrystals and other Lévy-walk processes, *Phys. Rev. Lett.* **94**, 080601 (2005).
- [52] G. Bel and E. Barkai, Weak ergodicity breaking in the continuous-time random walk, *Phys. Rev. Lett.* **94**, 240602 (2005).

- 384 [53] B. B. Mandelbrot and J. W. Van Ness, Fractional Brownian motions, fractional noises and applications, *SIAM Rev.* **10**,
385 422 (1968).
- 386 [54] J.-P. Bouchaud and A. Georges, Anomalous diffusion in disordered media: statistical mechanisms, models and physical
387 applications, *Phys. Rep.* **195**, 127 (1990).
- 388 [55] H. Scher and M. Lax, Stochastic transport in a disordered solid. I. Theory, *Phys. Rev. B* **7**, 4491 (1973).
- 389 [56] H. Scher, Continuous time random walk (CTRW) put to work, *Eur. Phys. J. B* **90**, 1 (2017).
- 390 [57] J. Klafter and I. M. Sokolov, First steps in random walks: from tools to applications (2011).
- 391 [58] T. Akimoto and E. Barkai, Aging generates regular motions in weakly chaotic systems, *Phys. Rev. E* **87**, 032915 (2013).
- 392 [59] J. H. Schulz, E. Barkai, and R. Metzler, Aging renewal theory and application to random walks, *Phys. Rev. X* **4**, 011028
393 (2014).
- 394 [60] E. J. Akin, L. Solé, B. Johnson, M. el Beheiry, J.-B. Masson, D. Krapf, and M. M. Tamkun, Single-molecule imaging of
395 Nav1.6 on the surface of hippocampal neurons reveals somatic nanoclusters, *Biophys. J.* **111**, 1235 (2016).
- 396 [61] K. Jaqaman, D. Loerke, M. Mettlen, H. Kuwata, S. Grinstein, S. L. Schmid, and G. Danuser, Robust single-particle
397 tracking in live-cell time-lapse sequences, *Nat. Methods* **5**, 695 (2008).
- 398 [62] A. Weron, K. Burnecki, E. J. Akin, L. Solé, M. Balcerek, M. M. Tamkun, and D. Krapf, Ergodicity breaking on the
399 neuronal surface emerges from random switching between diffusive states, *Sci. Rep.* **7**, 1 (2017).
- 400 [63] N. Leibovich and E. Barkai, $1/f^\beta$ noise for scale-invariant processes: how long you wait matters, *Eur. Phys. J. B* **90**, 1
401 (2017).
- 402 [64] Y. Meroz, I. M. Sokolov, and J. Klafter, Subdiffusion of mixed origins: when ergodicity and nonergodicity coexist, *Phys.*
403 *Rev. E* **81**, 010101 (2010).
- 404 [65] R. Schumer, D. A. Benson, M. M. Meerschaert, and B. Baeumer, Fractal mobile/immobile solute transport, *Water Resour.*
405 *Res.* **39** (2003).
- 406 [66] B. Berkowitz, A. Cortis, M. Dentz, and H. Scher, Modeling non-fickian transport in geological formations as a continuous
407 time random walk, *Rev. Geophys.* **44** (2006).
- 408 [67] O. Vilik, Y. Orchan, M. Charter, N. Ganot, S. Toledo, R. Nathan, and M. Assaf, Ergodicity breaking and lack of a typical
409 waiting time in area-restricted search of avian predators, arXiv preprint arXiv:2101.11527 (2021).

Figures

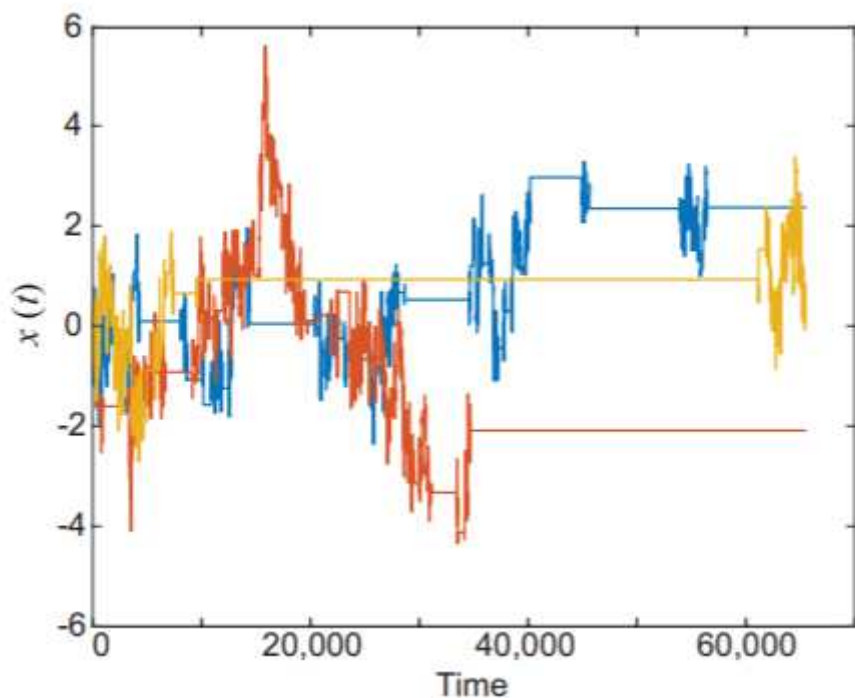


Figure 1

Three representative trajectories for a process subordinated to fractional Brownian motion, such that the Hurst exponent is $H = 0.3$ and the CTRW anomalous exponent is $\alpha = 0.8$. Long immobilization times are observed within the fractional Brownian motion.

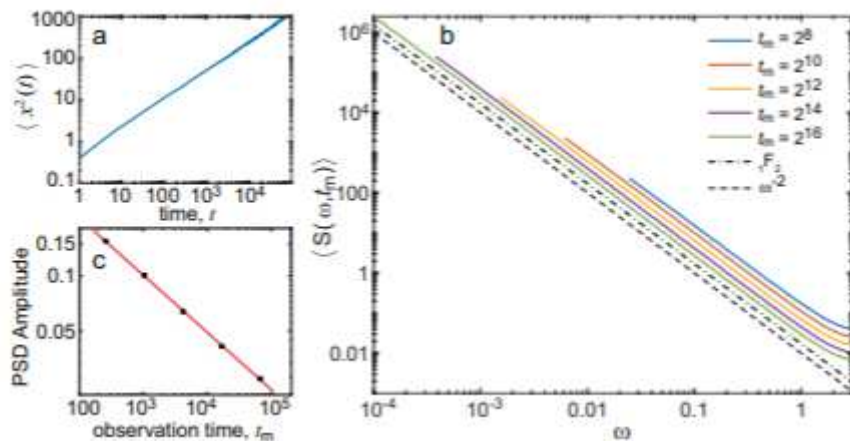


Figure 2

Results from numerical simulation of the CTRW, i.e. Brownian motion with power-law waiting times. The simulations were performed for $\alpha = 0.7$ and 10,000 realizations were obtained. [See Manuscript PDF file for full caption]

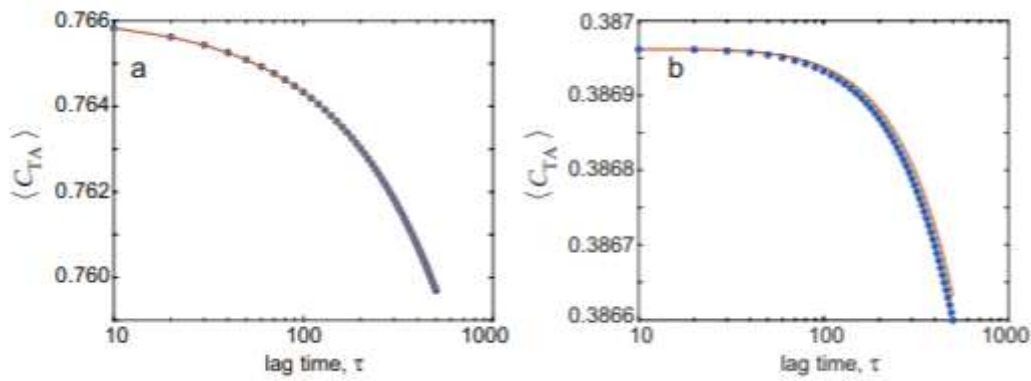


Figure 3

Numerical simulations agree with the time average-autocorrelation analytical results. [See Manuscript PDF file for full caption]

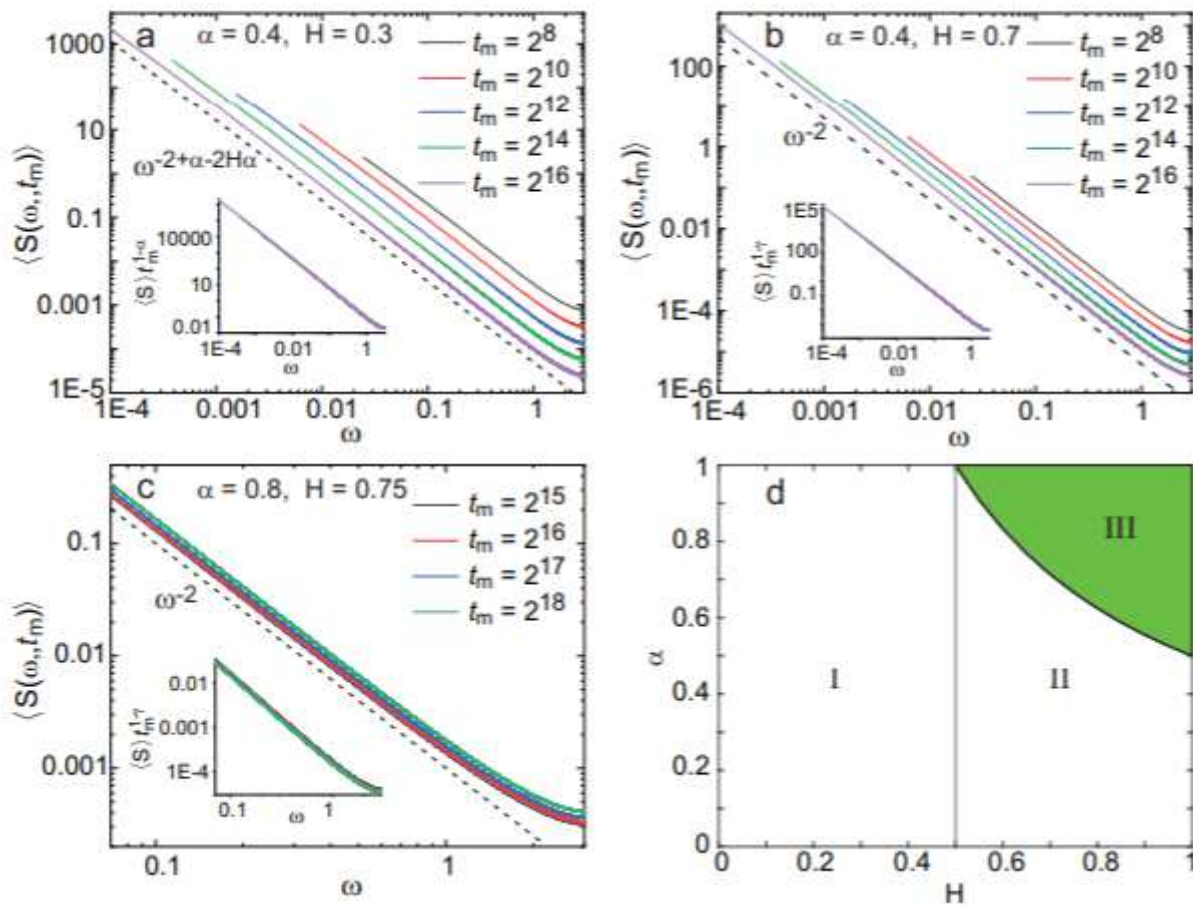


Figure 4

Power spectral density of numerical simulations of fBM with heavy-tailed immobilization times. [See Manuscript PDF file for full caption]

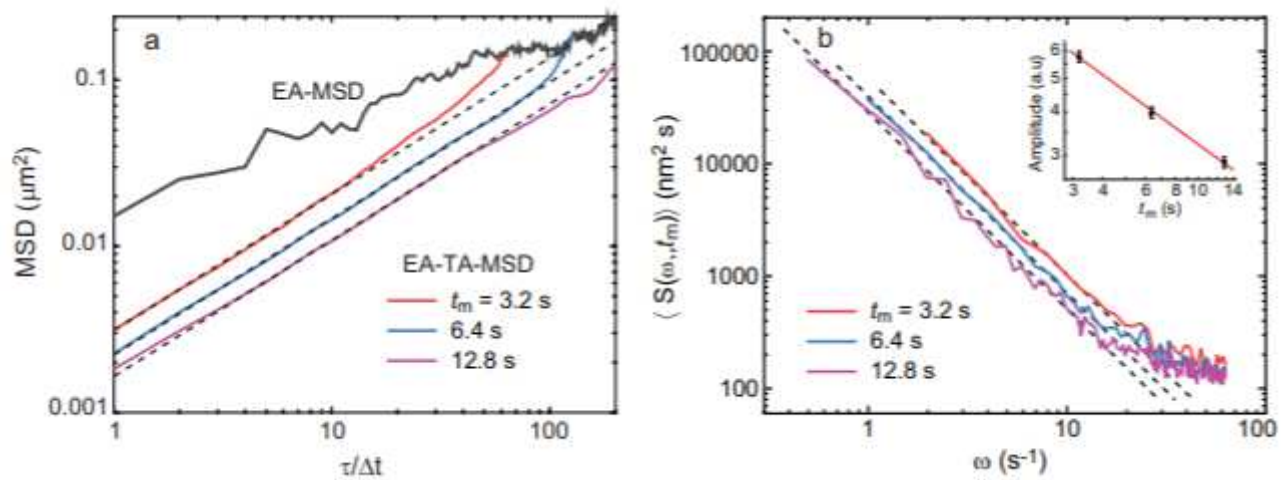


Figure 5

Analysis of Nav1.6 experimental trajectories in the soma of hippocampal neurons. [See Manuscript PDF file for full caption]

Supplementary Files

This is a list of supplementary files associated with this preprint. Click to download.

- [Supplement.pdf](#)